A Self-calibration Kalman Filter Algorithm for Dual-axis RINS Based on the Transverse Ellipsoidal Earth Model

Pengcheng Mu, Shilong Jin*, Zhikun Liao,
Zhonghong Liang, Yuanhan Wang, Lin Wang*
College of Advanced Interdisciplinary Studies, Nanhu Laser Laboratory
National University of Defense Technology, Changsha, China
mupengcheng@nudt.edu.cn, s_l_jin@hotmail.com, liaozhikun12@nudt.edu.cn,
wyuanhan@nudt.edu.cn, liangzhonghong@nudt.edu.cn, wanglin11@nudt.edu.cn

***Abstract*—The Kalman filter method plays a crucial role in enhancing the navigation accuracy of the dual-axis rotational inertial navigation system (RINS) through periodic estimation and compensation of device errors. Due to the particularity of polar geography, the traditional RINS mechanism in the local-level geographic frame loses efficacy in the polar region. This paper proposes a self-calibration Kalman filter algorithm based on the transverse ellipsoidal earth model to solve the self-calibration problem of RINS in polar region. This method firstly transforms the state of the local-level geographic frame to the transverse frame, and then constructs the prediction model and observation model of the Kalman filter based on the carrier state and error parameters in the transverse frame. In the self-calibration stage, a suitable rotation strategy is employed to stimulate the errors of RINS, and the proposed algorithm is utilized to estimate and compensate for the resulting errors. In addition, the traditional spherical earth model is improved to ellipsoidal earth model in this algorithm to avoid additional errors in the polar region. Monte Carlo experiments are carried out with simulation data at high latitudes, and then experiments at middle latitudes are carried out with ring laser gyro-based dual-axis RINS. The results demonstrate that the proposed method enables precise calibration of all error parameters, which aligns consistently with results obtained within the local-level geographic frame.**

***Index Terms*—Polar Region; Dual-axis RINS; Kalman Filter; Self-calibration; Transverse Frame;**

I. Introduction

Starp-down inertial navigation system (SINS) is widely used in marine navigation because of its autonomy, concealment, and anti-interference, which can provide full-scale motion information, including velocity, position, and attitude [1] [2]. The rotational inertial navigation system (RINS) is a significant advancement in inertial technology which is developed from the foundation of SINS. Because gyroscope and accelerometer bias can be modulated by periodically rotating the inertial measurement unit (IMU), this limits the accumulation of navigation errors in the RINS and enables its long-time navigation [3]–[5].

In the field of modern marine navigation, RINS as the core of navigation has been widely used in the middle and low latitudes [6] [7]. However, in polar navigation, some particularities differ from those of middle and low latitudes. The traditional RINS mechanism exhibits a significant increase in heading error at high latitudes due to the rapid convergence of meridians in the polar region, which indicates that the traditional local-level geographic frame is not suitable for polar region navigation. Scholars have conducted comprehensive research in response to this problem. The transverse frame (t frame) and grid frame (g frame), as two mainstream subdivisions of mechanism for the high latitude, have matured [8] [9]. The quantitative analysis in [10] illustrates that under certain conditions transverse frame SINS is equivalent to grid frame SINS. Cheng et al. [11] derived the nonlinear error model of the transverse frame based on the ellipsoidal earth model, and proposed an integrated alignment algorithm assisted by the transverse frame Doppler velocity log (DVL). This method successfully solves the problem of inaccurate course alignment caused by the overlap of the gravity vector and rotation vector in the polar region. Song et al. [12] proposed a SINS/CNS/GPS integrated navigation algorithm based on an indirect grid framework to solve the problem of insufficient accuracy of existing polar airborne navigation. Tian et al. [13] proposed a robust SINS/DVL integrated navigation algorithm in the transverse frame for the harsh polar environment's impact on DVL output. In addition, Wang et al. [14] used the grid frame as the navigation frame in the redundant RINS configuration of dual-axis RINS and single-axis RINS to improve the global navigation capability of ships.

The above briefly lists several branches of polar inertial navigation research, which can be summarized into three aspects: the new INS mechanism, polar integrated navigation, and polar alignment method. However, there is a lack of relevant research on the self-calibration method of inertial data errors compensation under long endurance conditions in polar region.

Self-calibration, also known as online calibration, is a convenient method to ensure the navigation performance of RINS, and has been widely studied by scholars in recent years [15]–[17]. One of the most effective self-calibration methods

is to use the Kalman filter to construct appropriate equations of state and observation to estimate the error of RINS. Hu et al. [18] proposed the concept of a virtual platform suitable for the self-calibration of the outer-azimuth tri-axis RINS. This platform addresses the issue of the excitation sequence used for the self-calibration of the inner-azimuth tri-axis RINS, which cannot be applied to the outer-azimuth tri-axis RINS. Wang et al. [19] proposed an novel self-calibration strategy for dual-axis RINS and conducted a thorough analysis in aspects such as error observability, separation principle, and rotation control. The simulation and experiment results indicated that all 21 error parameters included in the system could be well estimated. However, all the studies only consider the calibration problem in the middle and low latitudes, and carry out relevant studies based on the traditional local-level geographical frame, without considering the failure of the traditional local-level geographical frame in the polar region. Therefore, it is of great significance to develop the self-calibration technology of RINS in the polar region and compensate for the errors of inertial devices in time to ensure the safe polar navigation of ships.

In view of the above problems, a self-calibration Kalman filter algorithm for dual-axis RINS, designed for polar region, is proposed based on the transverse frame. The first step of the proposed algorithm is to identify the error parameters of the device that need to be calibrated. Then, the algorithm provides the RINS mechanism and self-calibration Kalman filter equation in the transverse frame. In addition, the conventional spherical earth model is replaced by the ellipsoidal earth model to reduce additional model errors. The effectiveness of the proposed algorithm is verified by the Monte Carlo simulation experiment and actual inertial navigation experiment, respectively.

The rest of this paper is organized as follows: Section II explains the concept of the transverse system and the mechanism of RINS. In the Section III, a self-calibration Kalman filter algorithm is designed for RINS to improve navigation accuracy. In the Section IV, both a Monte Carlo simulation experiment and a real experiment are conducted. The conclusion is presented in section V.

II. TRANSVERSE FRAME DEFINITION AND RINS NAVIGATION MECHANISM

A. Definition of the Transverse Frame

The transverse frame includes the transverse earth frame and the transverse geographic frame. Under the reference frame of the transverse frame, the transverse polar axis, the transverse equatorial plane, the transverse prime meridian plane, and the transverse latitude and longitude need to be redefined.

As shown in Fig. 1, the transverse earth frame is denoted by the e' frame. The e' frame can be defined through two sequence rotations of the earth-centered earth-fixed frame, i.e., e frame. Namely, the e frame is rotated -90° around its x_e axis, then rotated -90° around the intermediate z_e axis. The direction cosine matrix (DCM) between them can be written as (1), where γ = -90°.

$$C_e^{e'} = \begin{bmatrix} \cos(\gamma) & \sin(\gamma) & 0 \\ -\sin(\gamma) & \cos(\gamma) & 0 \\ 0 & 0 & 1 \end{bmatrix} \begin{bmatrix} 1 & 0 & 0 \\ 0 & \cos(\gamma) & \sin(\gamma) \\ 0 & -\sin(\gamma) & \cos(\gamma) \end{bmatrix} = \begin{bmatrix} 0 & 0 & 1 \\ 1 & 0 & 0 \\ 0 & 1 & 0 \end{bmatrix} \tag{1}$$

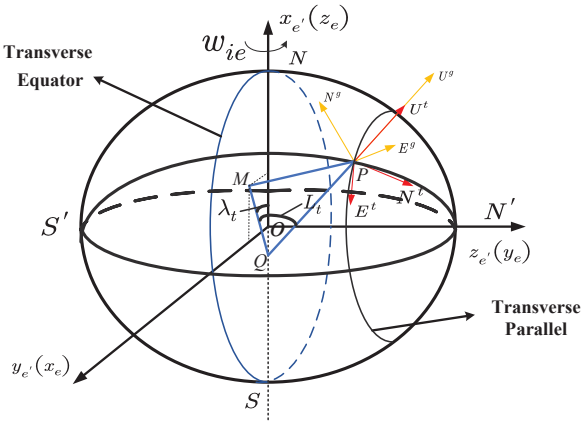

Fig. 1. Transverse frame

In this paper, the i frame, b frame, and the g frame respectively represent the inertial frame, the body frame of the carrier, and the navigation frame (local-level geographic frame), with tri-axes denoted by E^g, N^g, U^g (x_g axis, y_g axis, and z_g axis). The transverse ellipsoidal earth model defines the meridian circle of the 0° and 180° as the transverse equator ($Ox_{e'}y_{e'}$), and the meridian circle of the 90°E and 90°W as the transverse prime meridian ($Ox_{e'}z_{e'}$), the intersection point between the 90°E meridian and equator as the transverse north pole (N') [20]. The transverse longitude and latitude are determined by the angle between the vertical line and each plane. At point P, the transverse latitude L^t is the angle between the PQ and the transverse equatorial plane. The transverse longitude λ^t is the angle between the MQ and $x_{e'}$ axes, where M is the projection of P on the equatorial plane. The Q represents the intersection of the position of a carrier in the transverse frame and the extension line of the origin on the transverse equator.

The DCM from the e frame to the g frame is written as:

$$C_e^g = \begin{bmatrix} -\sin\lambda & \cos\lambda & 0 \\ -\sin L\cos\lambda & -\sin L\sin\lambda & \cos L \\ \cos L\cos\lambda & \cos L\sin\lambda & \sin L \end{bmatrix} \tag{2}$$

where L is the traditional latitude and λ the traditional longitude.

The DCM from the e' frame to the t frame is written as:

$$C_{e'}^t = \begin{bmatrix} -\sin\lambda^t & \cos\lambda^t & 0 \\ -\sin L^t\cos\lambda^t & -\sin L^t\sin\lambda^t & \cos L^t \\ \cos L^t\cos\lambda^t & \cos L^t\sin\lambda^t & \sin L^t \end{bmatrix} \tag{3}$$

From the above, DCM from g frame to t frame can be written as:

$$\boldsymbol{C}_g^t = \boldsymbol{C}_{e'}^t \boldsymbol{C}_e^{e'} \boldsymbol{C}_g^e = \begin{bmatrix} \cos\beta & -\sin\beta & 0 \\ \sin\beta & \cos\beta & 0 \\ 0 & 0 & 1 \end{bmatrix} \tag{4}$$

There is an angle β between the transverse north reference and the traditional north reference in the defined transverse local-level geographic frame, where β can be represented as:

$$\cos\beta = \frac{-\sin L \sin\lambda}{\sqrt{1-\cos^2 L \sin^2\lambda}} = \frac{-\sin L^t \sin\lambda^t}{\sqrt{1-\cos^2 L^t \cos^2\lambda^t}} \tag{5}$$

$$\sin\beta = \frac{\cos\lambda}{\sqrt{1-\cos^2 L \sin^2\lambda}} = \frac{\sin L^t}{\sqrt{1-\cos^2 L^t \cos^2\lambda^t}} \tag{6}$$

The relationships between the transverse latitude and traditional latitude, as well as the transverse longitude and the traditional longitude, are as follows:

$$L^t = \arctan\left(\frac{\cos L \sin\lambda}{\sqrt{1-\cos^2 L \sin^2\lambda}}\right) \tag{7}$$

$$\lambda^t = \arctan\left(\frac{\cos\lambda}{\tan L}\right) \tag{8}$$

B. Transverse Frame RINS Mechanism

The attitude update equation in the transverse geographic frame is formulated as:

$$\dot{\boldsymbol{C}}_b^t = \boldsymbol{C}_b^t \left[\boldsymbol{w}_{ib}^b \times\right] - \left[\boldsymbol{w}_{it}^t \times\right] \boldsymbol{C}_b^t \tag{9}$$

where $\boldsymbol{C}_b^t$ is the direction cosine matrix from the b frame to the t frame, $\boldsymbol{w}_{ib}^b$ is the angular velocity of the b frame relative to the i frame as measured by the gyroscope assembly, $[\cdot\times]$ is the symmetric matrix of vector $\cdot$, and $\boldsymbol{w}_{it}^t$ is the angular velocity of the t frame relative to the i frame, which can be expressed as:

$$\boldsymbol{w}_{it}^t = \boldsymbol{w}_{ie'}^t + \boldsymbol{w}_{e't}^t \tag{10}$$

with

$$\boldsymbol{w}_{ie'}^t = \boldsymbol{C}_{e'}^t \begin{bmatrix} w_{ie} & 0 & 0 \end{bmatrix}^T \tag{11}$$

$$\boldsymbol{w}_{e't}^t = \begin{bmatrix} \dfrac{1}{\tau} & -\dfrac{1}{R_y} \\ \dfrac{1}{R_x} & -\dfrac{1}{\tau} \\ \dfrac{\tan L^t}{R_x} & -\dfrac{\tan L^t}{\tau} \end{bmatrix} \begin{bmatrix} v_E^t \\ v_N^t \end{bmatrix} \tag{12}$$

where $\boldsymbol{w}_{ie'}^t$ is the angular velocity of the e' frame relative to the i frame, $\boldsymbol{w}_{e't}^t$ is the angular velocity of the t frame relative to the e' frame, w_{ie} is the earth rotation rate, R_x is the radius of the curvature along the x axis, R_y is the radius of the curvature along the y axis, τ is the twist rate of the ellipsoid, v_E^t is the transverse east velocity, and v_N^t is the transverse north velocity.

$$\frac{1}{R_x} = \frac{\sin^2\beta}{R_N+h} + \frac{\cos^2\beta}{R_E+h} \tag{13}$$

$$\frac{1}{R_y} = \frac{\cos^2\beta}{R_N+h} + \frac{\sin^2\beta}{R_E+h} \tag{14}$$

$$\frac{1}{\tau} = \left(\frac{1}{R_N+h} - \frac{1}{R_E+h}\right)\sin\beta\cos\beta \tag{15}$$

$$R_E = \frac{R_e}{\sqrt{1-e^2\cos^2 L^t \cos^2\lambda^t}} \tag{16}$$

$$R_N = \frac{R_e\left(1-e\right)^2}{\left(1-e^2\cos^2 L^t\cos^2\lambda^t\right)^{\frac{3}{2}}} \tag{17}$$

where e is the eccentricity of the earth and R_e is the earth semi-major axis radius.

The velocity update equation in the transverse geographic frame is expressed as:

$$\dot{\boldsymbol{v}}^t = \boldsymbol{C}_b^t \boldsymbol{f}^b - \left(2\boldsymbol{w}_{ie'}^t + \boldsymbol{w}_{e't}^t\right) \times \boldsymbol{v}^t + \boldsymbol{g}^t \tag{18}$$

where $\boldsymbol{v}^t = \begin{bmatrix} v_E^t & v_N^t & v_U^t \end{bmatrix}^T$ is the RINS velocity in the transverse frame, $\boldsymbol{f}^b$ is the specific force measured by the accelerometer assembly, and g^t denotes the gravity vector.

The position update equation in the transverse geographic frame is written as:

$$\dot{L}^t = -\frac{1}{\tau} v_E^t + \frac{1}{R_y} v_N^t \tag{19}$$

$$\dot{\lambda}^t = \frac{1}{R_x \cos L^t} v_E^t - \frac{1}{\tau \cos L^t} v_N^t \tag{20}$$

III. SELF-CALIBRATION KALMAN FILTER ALGORITHM FOR RINS BASED ON THE TRANSVERSE FRAME

A. RINS Error Model

Taking into account the constant biases of the inertial sensors, installation errors, and scale factor errors, the error model for the gyroscope and accelerometer can be expressed as:

$$\delta\boldsymbol{w}_{ib}^b = \left(\delta\boldsymbol{\kappa}_g + \delta\boldsymbol{\mu}_g\right)\boldsymbol{w}_{ib}^b + \boldsymbol{\varepsilon}^b + \boldsymbol{w}_\varepsilon^b \tag{21}$$

$$\delta\boldsymbol{f}^b = \left(\delta\boldsymbol{\kappa}_a + \delta\boldsymbol{\mu}_a\right)\boldsymbol{f}^b + \boldsymbol{\nabla}^b + \boldsymbol{w}_\nabla^b \tag{22}$$

where $\delta\boldsymbol{w}_{ib}^b$ and $\delta\boldsymbol{f}^b$ represent the errors in angular velocity and specific force projected in the b frame, respectively. $\boldsymbol{w}_{ib}^b = \begin{bmatrix} w_{ibx}^b & w_{iby}^b & w_{ibz}^b \end{bmatrix}^T$ and $\boldsymbol{f}^b = \begin{bmatrix} f_x^b & f_y^b & f_z^b \end{bmatrix}^T$ denote the angular velocity and specific force inputs, respectively. $\boldsymbol{\varepsilon}^b = \begin{bmatrix} \varepsilon_x^b & \varepsilon_y^b & \varepsilon_z^b \end{bmatrix}^T$ represents the constant gyroscope drifts, and $\boldsymbol{\nabla}^b = \begin{bmatrix} \nabla_x^b & \nabla_y^b & \nabla_z^b \end{bmatrix}^T$ represents the constant accelerometer biases. $\boldsymbol{w}_\varepsilon^b$ and $\boldsymbol{w}_\nabla^b$ denote the white noise of the gyroscope and accelerometer, respectively.

The gyroscope scale factor error matrix and the accelerometer scale factor error matrix can be expressed as:

$$\delta\boldsymbol{\kappa}_g = \begin{bmatrix} \delta\kappa_{gx} & 0 & 0 \\ 0 & \delta\kappa_{gy} & 0 \\ 0 & 0 & \delta\kappa_{gz} \end{bmatrix} \quad \delta\boldsymbol{\kappa}_a = \begin{bmatrix} \delta\kappa_{ax} & 0 & 0 \\ 0 & \delta\kappa_{ay} & 0 \\ 0 & 0 & \delta\kappa_{az} \end{bmatrix} \tag{23}$$

where $\delta\kappa_{gi}, \delta\kappa_{ai}$ (for $i = x, y, z$) denote the scale factor errors of the corresponding gyroscope and accelerometer along a certain axis, respectively.

Given that the installation error angle of the RINS cannot be entirely decoupled, the b frame is based on the constraints imposed by the gyroscope-sensitive axes to guarantee the uniqueness of calibration results. The installation error matrices $\delta\boldsymbol{\mu}_g$ and $\delta\boldsymbol{\mu}_a$ can be represented as follows:

$$\delta\boldsymbol{\mu}_g = \begin{bmatrix} 0 & 0 & 0 \\ \delta\mu_{gyx} & 0 & 0 \\ \delta\mu_{gzx} & \delta\mu_{gzy} & 0 \end{bmatrix} \quad \delta\boldsymbol{\mu}_a = \begin{bmatrix} 0 & \delta\mu_{axy} & \delta\mu_{axz} \\ \delta\mu_{ayx} & 0 & \delta\mu_{ayz} \\ \delta\mu_{azx} & \delta\mu_{azy} & 0 \end{bmatrix} \tag{24}$$

where the non-zero elements in $\delta\boldsymbol{\mu}_g, \delta\boldsymbol{\mu}_a$ represent the installation error angles of the gyroscope and accelerometer, respectively.

B. Kalman Filter Model Design For Proposed Self-Calibration Method

In this paper, the error propagation characteristics of the RINS in the transverse frame are described in:

$$\dot{\boldsymbol{\phi}}^t = -\boldsymbol{w}_{it}^t \times \boldsymbol{\phi}^t + \delta\boldsymbol{w}_{it}^t - \boldsymbol{C}_b^t \delta\boldsymbol{w}_{ib}^b \tag{25}$$

$$\begin{aligned} \delta\dot{\boldsymbol{v}}^t = {} & \boldsymbol{f}^t \times \boldsymbol{\phi}^t - \left(2\boldsymbol{w}_{ie\prime}^t + \boldsymbol{w}_{e\prime}^t\right) \times \delta\boldsymbol{v}^t \\ & + \boldsymbol{v}^t \times \left(2\delta\boldsymbol{w}_{ie\prime}^t + \delta\boldsymbol{w}_{e\prime t}^t\right) + \boldsymbol{C}_b^t \delta\boldsymbol{f}_{ib}^b \end{aligned} \tag{26}$$

$$\delta\dot{L}^t = -\frac{1}{\tau}\delta v_E^t + \frac{1}{R_y}\delta v_N^t \tag{27}$$

$$\begin{aligned} \delta\dot{\lambda}^t = {} & \frac{1}{R_x \cos L^t}\delta v_E^t - \frac{1}{\tau \cos L^t}\delta v_N^t \\ & + \frac{\tan L^t}{\cos L^t}\left(\frac{v_E^t}{R_x} - \frac{v_N^t}{\tau}\right)\delta L^t \end{aligned} \tag{28}$$

$$\delta\dot{h} = \delta v_U^t \tag{29}$$

where $\boldsymbol{\phi}^t = \begin{bmatrix} \phi_E^t & \phi_N^t & \phi_U^t \end{bmatrix}^T$ represents the attitude error in the t frame, and $\delta\boldsymbol{v}^t = \begin{bmatrix} \delta v_E^t & \delta v_N^t & \delta v_U^t \end{bmatrix}^T$ denotes the velocity error in the t frame. δL^t, $\delta\lambda^t$, and δh denote the errors in transverse latitude, longitude, and height, respectively.

In this paper, the basic Kalman filter method is used for dual-axis RINS calibration. The system state equation and measurement equation are as follows.

1)$State\ Equation$: The Kalman filter calibration equation is formulated as follows:

$$\dot{\boldsymbol{X}} = \boldsymbol{F}\boldsymbol{X} + \boldsymbol{G}\boldsymbol{W} \tag{30}$$

where $\boldsymbol{X}$ represents the state vector, $\boldsymbol{W}$ is the system noise matrix associated with gyroscope and accelerometer:

$$W = \begin{bmatrix} w_{\varepsilon x}^b & w_{\varepsilon x}^b & w_{\varepsilon x}^b & w_{\nabla x}^b & w_{\nabla y}^b & w_{\nabla z}^b \end{bmatrix}^T \tag{31}$$

The state vector is defined as follows:

$$\boldsymbol{X} = \begin{bmatrix} \phi_E^t & \phi_N^t & \phi_U^t & \delta v_E^t & \delta v_N^t & \delta v_U^t \\ \delta L^t & \delta\lambda^t & \delta h & \varepsilon_x^b & \varepsilon_y^b & \varepsilon_z^b \\ \nabla_x^b & \nabla_y^b & \nabla_z^b & \delta\kappa_{gx} & \delta\mu_{gyx} & \delta\mu_{gzx} \\ \delta\kappa_{gy} & \delta\mu_{gzy} & \delta\kappa_{gz} & \delta\kappa_{ax} & \delta\mu_{ayx} & \delta\mu_{azx} \\ \delta\mu_{axy} & \delta\kappa_{ay} & \delta\mu_{azy} & \delta\mu_{axz} & \delta\mu_{ayz} & \delta\kappa_{az} \end{bmatrix}^T \tag{32}$$

The system matrix $\boldsymbol{F}$ and the noise matrix $\boldsymbol{G}$ can be given by the error equations(25)-(29).

2)$Measurement\ Equation$: During the calibration process, the actual velocity and position of RINS remain unchanged. Therefore, the measurement equation with velocity error and position error can be written as:

$$\begin{aligned} \boldsymbol{Z} &= \begin{bmatrix} \delta v_E^t & \delta v_N^t & \delta v_U^t & \delta L^t & \delta\lambda^t & \delta h \end{bmatrix}^T \\ &= \boldsymbol{H}\boldsymbol{X} + \boldsymbol{V} \end{aligned} \tag{33}$$

where $\boldsymbol{V}$ represents the measurement noise, and the expression of the measurement matrix $\boldsymbol{H}$ is as follows:

$$\boldsymbol{H} = \begin{bmatrix} \boldsymbol{0}_{6\times3} & \boldsymbol{I}_{6\times6} & \boldsymbol{0}_{6\times21} \end{bmatrix} \tag{34}$$

where $\boldsymbol{I}$ denotes the identity matrix.

C. Observability Analysis

The observability of the state of the system is a crucial factor for its convergence. The observability of each state variable is qualitatively analyzed using piece-wise constant system (PWCS) [21]. PWCS uses the stripped observability matrix (SOM) instead of the total observability matrix (TOM) to calculate the rank of SOM at each position of the path. If the rank of SOM reaches the dimension of the system state variable, the system is considered to be fully observable. The system equation for each time interval can be expressed as:

$$\begin{cases} \dot{\boldsymbol{X}} = \boldsymbol{F}_j\boldsymbol{X} \\ \boldsymbol{Z} = \boldsymbol{H}_j\boldsymbol{X} \end{cases} \tag{35}$$

where j(j=1,2...r) indicates the number of time segments. The observability matrix of the system in the jth period is expressed as:

$$\boldsymbol{Q}_j^T = \begin{bmatrix} (\boldsymbol{H}_j)^T & (\boldsymbol{H}_j\boldsymbol{F}_j)^T & \left(\boldsymbol{H}_j\boldsymbol{F}_j^2\right)^T \cdots \left(\boldsymbol{H}_j\boldsymbol{F}_j^{n-1}\right)^T \end{bmatrix} \tag{36}$$

where n represents the system dimension. The system's SOM is expressed as:

$$\tilde{\boldsymbol{Q}}_{SOM}(r) = \begin{bmatrix} \boldsymbol{Q}_1 & \boldsymbol{Q}_2 \cdots \boldsymbol{Q}_r \end{bmatrix}^T \tag{37}$$

Fig.2 shows the observability analysis results of the system during the 19-position calibration scheme [22]. At the beginning, the rank of the SOM is 12, which means that there are 12 states of the system that can be observed. As the rotation progresses, at the sixth position, the SOM reaches full rank, so that all state quantities in the system can be observed.

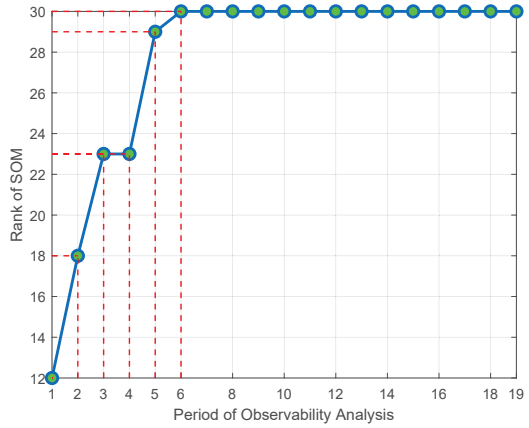

Fig. 2. Rank of the SOM

IV. Experimental Result and Discussion

A. Monte Carlo Polar Simulation

To replicate the high-latitude surroundings as accurately as possible, the simulation experiment is conducted in a high-latitude area with coordinates (86°N, 113°E). Five hundred repeated experiments are carried out using the Monte Carlo method to verify the absolute accuracy of the algorithm proposed in this paper. The errors model of the dual-axis RINS is determined by (21)-(22), with Table I providing the corresponding value settings for each error parameter.

TABLE I
Error Parameters of RINS

Error Parameters	Values
Gyroscope drift	0.01 °/h
Gyroscope angular random walk (ARW)	$0.0005°/\sqrt{h}$
Accelerometer bias	50 ug
Power spectral density (PSD) of accelerometer noise	$5ug/\sqrt{Hz}$
$\delta\kappa_{gx}$,$\delta\kappa_{gy}$,$\delta\kappa_{gz}$	-12ppm,-6ppm,-8ppm
$\delta\kappa_{ax}$,$\delta\kappa_{ay}$,$\delta\kappa_{az}$	-30ppm,-40ppm,-50ppm
$\delta\mu_{gyx}$,$\delta\mu_{gzx}$,$\delta\mu_{gzy}$	-30″,-40″,50″
$\delta\mu_{ayx}$,$\delta\mu_{azx}$,$\delta\mu_{azy}$ $\delta\mu_{axy}$,$\delta\mu_{axz}$,$\delta\mu_{ayz}$	-50″,-40″,-30″ 50″,40″,30″

The 19-position scheme is used to calibrate the dual-axis RINS, which rotates at a speed of 9° per second and remains static for 180 seconds after the rotation. To simulate the output of a marine inertial navigation system in real sea conditions, the carrier is assumed to swing around three axes at different frequencies. The wave motion in this experiment follows (38).

$$\begin{cases} \theta = 2^\circ \sin\left(2\pi/30 + \pi/4\right) \\ \gamma = 3^\circ \sin\left(2\pi/20 + \pi/3\right) \\ \psi = 2^\circ \sin\left(2\pi/100 + 2\pi/3\right) \end{cases} \tag{38}$$

In the above (38), θ, γ and ψ are pitch, roll and yaw of the carrier respectively. The above experimental conditions are utilized to conduct the Monte Carlo simulation experiments, resulting in the generation of a histogram depicting the distribution of estimated error parameters.

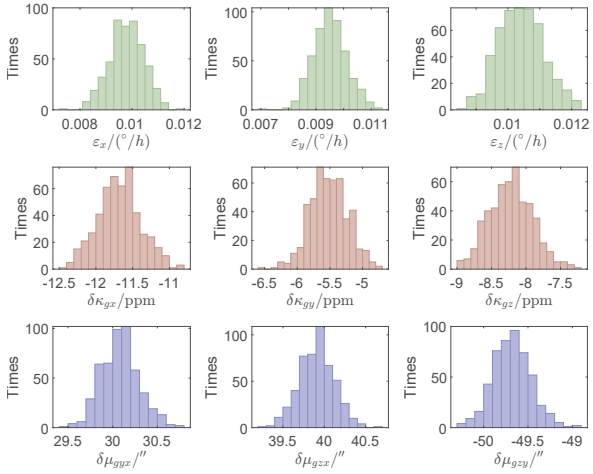

Fig. 3. Histogram of gyroscope error parameters estimation value distribution

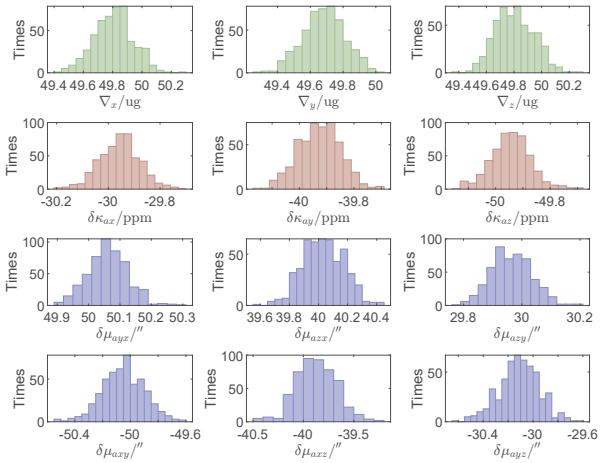

Fig. 4. Histogram of accelerometer error parameters estimation value distribution

As depicted in Fig.3 and Fig.4, the calibration results exhibit a normal distribution across 500 sets of repeated experiments due to the implementation of white noise for both gyroscopes and accelerometers. Notably, each error's calibration outcome converges towards its designated value, indicating excellent repeatability of the algorithm proposed in this paper.

In order to quantitatively analyze the algorithm's calibration accuracy, Table II presents the estimation mean value, maximum error, and root mean square error (RMSE) derived from Monte Carlo simulation results. It can be seen from the Table II that the calibration results of the proposed algorithm under the polar simulation data are highly consistent with the set error parameters, showing a good error estimation ability.

TABLE II
STATISTICAL CALIBRATION RESULTS OF PARAMETERS

Parameters	Real values	Estimation mean	Maximum error	RMSE
ε_x	0.01 °/h	0.0098 °/h	0.0026°/h	0.0006°/h
ε_y	0.01 °/h	0.0095 °/h	0.0029°/h	0.0006°/h
ε_z	0.01 °/h	0.0104 °/h	0.0023°/h	0.0007°/h
∇_x	50 ug	49.8068 ug	0.5667 ug	0.1323 ug
∇_y	50 ug	49.6828 ug	0.7077 ug	0.1266 ug
∇_z	50 ug	49.8052 ug	0.6384 ug	0.1405 ug
$\delta\kappa_{gx}$	-12 ppm	-11.6800 ppm	1.1738 ppm	0.2920 ppm
$\delta\kappa_{gy}$	-6 ppm	-5.5203 ppm	1.2964 ppm	0.2871 ppm
$\delta\kappa_{gz}$	-8 ppm	-8.2158 ppm	0.9842 ppm	0.3152 ppm
$\delta\kappa_{ax}$	-30 ppm	-29.9563 ppm	0.2954 ppm	0.0778 ppm
$\delta\kappa_{ay}$	-40 ppm	-39.9267 ppm	0.3045 ppm	0.0766 ppm
$\delta\kappa_{az}$	-50 ppm	-49.9435 ppm	0.3153 ppm	0.0728 ppm
$\delta\mu_{gyx}$	30 ″	30.0813 ″	0.7282 ″	0.2099 ″
$\delta\mu_{gzx}$	40 ″	39.9108 ″	0.7304 ″	0.2089 ″
$\delta\mu_{gzy}$	-50 ″	-49.6808 ″	1.0192 ″	0.2135 ″
$\delta\mu_{ayx}$	50 ″	50.0616 ″	0.2963 ″	0.0631 ″
$\delta\mu_{azx}$	40 ″	40.0328 ″	0.4374 ″	0.1411 ″
$\delta\mu_{azy}$	30 ″	29.9654 ″	0.2200 ″	0.0703 ″
$\delta\mu_{axy}$	-50 ″	-50.0498 ″	0.5483 ″	0.1524 ″
$\delta\mu_{axz}$	-40 ″	-39.8730 ″	0.7817 ″	0.1993 ″
$\delta\mu_{ayz}$	-30 ″	-30.1124 ″	0.6042 ″	0.1605 ″

B. Experiments

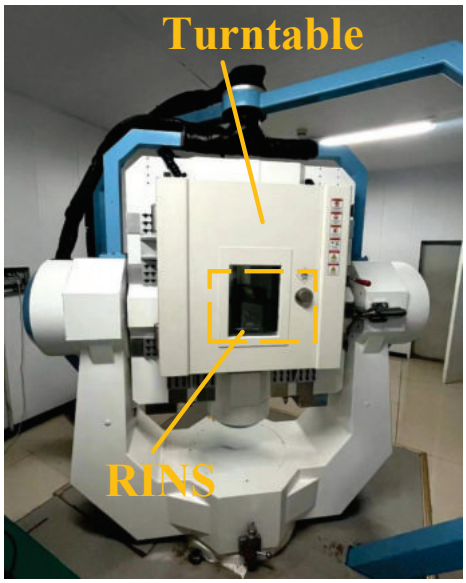

Fig. 5. Experimental platform

To validate the effectivity of the self-calibration method proposed in this paper, ring laser gyro-based dual-axis RINS is employed for testing. The 19-position calibration scheme is utilized as proposed in the literature [22]. This scheme can effectively excite the calibration of all error parameters in the RINS and has been validated as an efficient calibration method. The rotational velocity is set at 9°/s, with a pause of 180s at each position, and the entire process lasts approximately 4.5 hours. Experimental equipment includes high-precision ring laser gyro inertial navigation system and a turntable rotating around two axes. Fig.5 displays the experimental platform used in this paper.

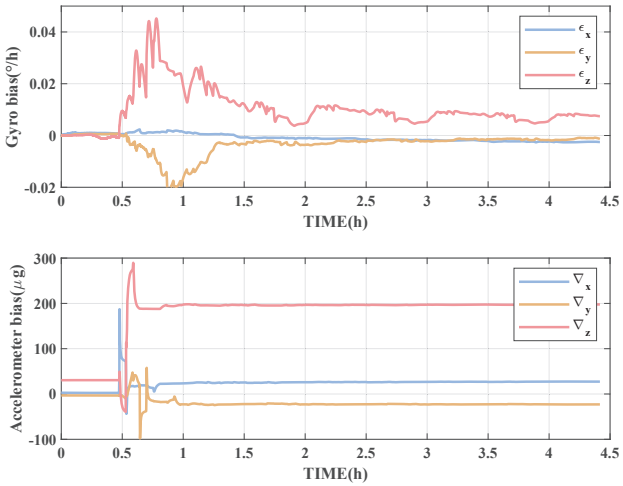

Fig. 6. Results of bias

Fig.6 shows the bias estimation curves for the gyroscope and accelerometer. The deviations for the gyroscope are 0.0025°/h, 0.0013°/h, and 0.0075°/h, respectively. Similarly, the accelerometer deviations are 27.2972ug, 22.9603ug, and 197.7258ug, respectively. Fig.7 displays the curve that results from estimating the installation error of gyroscopes and accelerometers. The installation errors of the gyroscopes are 0.2331 ″, -3.1490 ″, and 8.0787 ″, respectively. Additionally, the installation errors of the accelerometers are -0.3791 ″, -2.0838 ″, 5.5406 ″, -4.6813 ″, 3.9130 ″, and -7.1391 ″, respectively. Fig.8 displays the scale factor errors of the gyroscopes and accelerometers. After calibration, the gyroscopes have a scale factor errors of 1.0904 ppm, -2.5651 ppm, and -4.0995 ppm, while the accelerometers have a scale factor errors of -71.3529 ppm, -35.6156 ppm, and -163.6798 ppm. As seen from Fig.6-Fig.8, each error parameter converges to a stable value within the calibration time. In order to validate the accuracy of the proposed calibration algorithm, a comparison is made with the traditional calibration method.

The calibration results of the proposed algorithm and the traditional algorithm in local-level geographic frame are shown in Table III. The gyroscope drifts exhibit high consistency between the two methods, with a difference of less than 0.0005 °/h. The estimation error for accelerometer biases remains below 0.01 μg, and there is minimal disparity observed between them. The errors of the three-axis scale factor of the gyroscope calculated by the two methods are less than 0.25ppm. Similarly, the three-axis installation errors of the gyroscope in the two methods vary by 0.0898 ″, 0.1883 ″, and 0.1671 ″, respectively. The accelerometers' scale factor

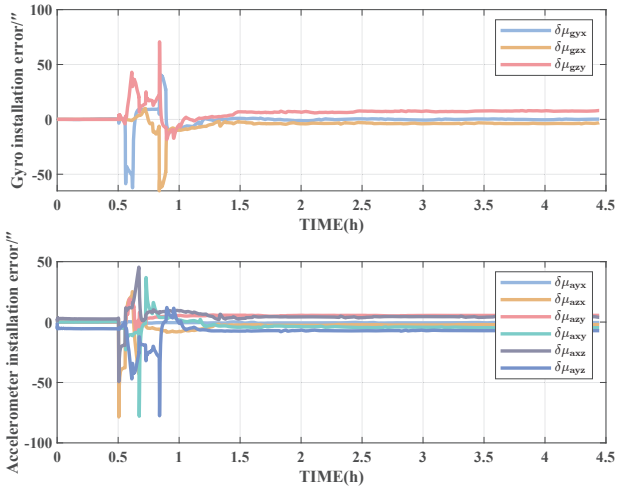

Fig. 7. Results of installation error

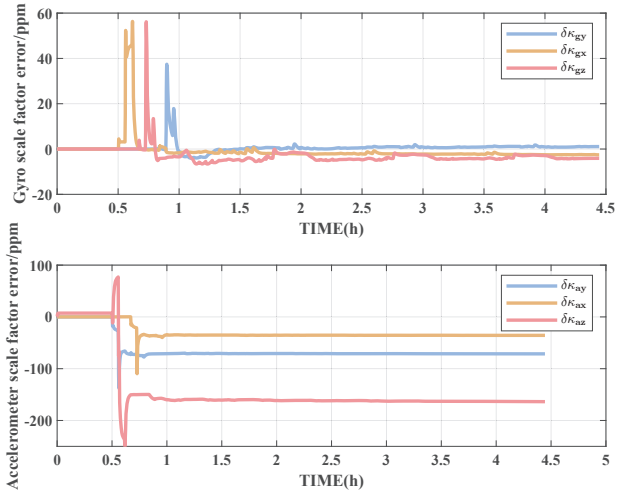

Fig. 8. Results of scale error

and installation errors are approximately 0.001 ppm and 0.1 ″, respectively. The calibration results of dual-axis RINS show that the calibration results based on the proposed algorithm are consistent with those based on the traditional geographic system at middle and low latitudes.

The errors obtained by the proposed algorithm are compensated to the raw data, and the pure inertial navigation based on the transverse frame is realized. The positioning errors are shown in Fig.9, which depicts the latitude and longitude errors of inertial data with compensated and uncompensated errors under static pure inertial navigation, with a running time of more than 11 hours. When the errors are not compensated, the latitude error and longitude error obtained by pure inertial navigation are 4045.8 meters and 3107.18 meters, respectively. After error compensation, the latitude error is 1433.53 m, and the longitude error is 1100.15 m, which are reduced by 2612.27 meters and 2007.03 meters, respectively. The positioning error calculated after error compensation is 1807.01

TABLE III
COMPARISON OF CALIBRATION RESULTS BETWEEN TRANSVERSE AND GEOGRAPHIC FRAMES FOR RING LASER GYRO-BASED DUAL-AXIS RINS

Parameters		Transverse frame	Geographic frame
Gyroscope Drift	ε_x	0.0025 °/h	0.0024 °/h
	ε_y	0.0013 °/h	0.0008 °/h
	ε_z	0.0075 °/h	0.0080 °/h
Accelerometer Bias	∇_x	27.2972 ug	27.2116 ug
	∇_y	22.9603 ug	22.9265 ug
	∇_z	197.7258 ug	197.7022 ug
Gyroscope Scale Factor Error	$\delta\kappa_{gx}$	1.0900 ppm	1.1205 ppm
	$\delta\kappa_{gy}$	-2.5653 ppm	-2.7787 ppm
	$\delta\kappa_{gz}$	-4.0992 ppm	-4.1565 ppm
Accelerometer Scale Factor Error	$\delta\kappa_{ax}$	-71.3529 ppm	-71.3543 ppm
	$\delta\kappa_{ay}$	-35.6156 ppm	-35.6182 ppm
	$\delta\kappa_{az}$	-163.6798 ppm	-163.6721 ppm
Gyroscope Installation Error	$\delta\mu_{gyx}$	0.2331 ″	0.3229 ″
	$\delta\mu_{gzx}$	-3.1490 ″	-2.9607 ″
	$\delta\mu_{gzy}$	8.0787 ″	7.9116 ″
Accelerometer Installation Error	$\delta\mu_{ayx}$	-0.3791 ″	-0.3758 ″
	$\delta\mu_{azx}$	-2.0838 ″	-2.0687 ″
	$\delta\mu_{axy}$	5.5406 ″	5.5147 ″
	$\delta\mu_{azy}$	-4.6813 ″	-4.6853 ″
	$\delta\mu_{axz}$	3.9130 ″	3.7925 ″
	$\delta\mu_{ayz}$	-7.1391 ″	-7.0652 ″

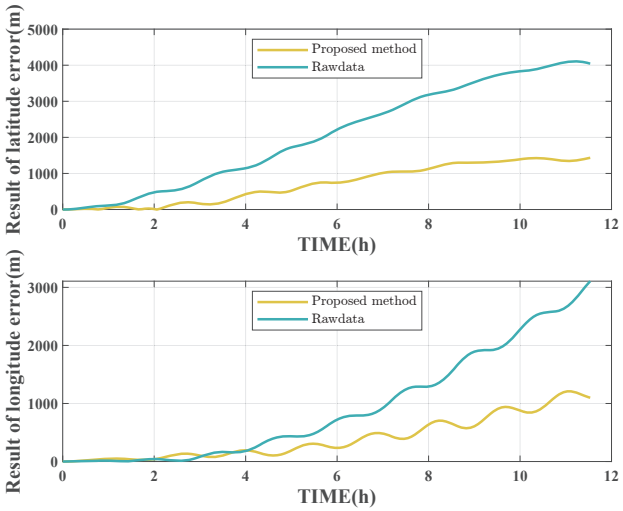

Fig. 9. Calculated latitude and longitude errors

meters, which is reduced by 3294.27m compared with the positioning error obtained from the raw data, as shown in Fig.10.

V. CONCLUSIONS

This paper presents a self-calibration Kalman filter algorithm for the transverse frame using the ellipsoidal earth model. The algorithm includes a 30-dimensional Kalman filter, and it provides the state model and measurement model, which can calibrate the error parameters of RINS. The effectiveness of the proposed algorithm is verified by

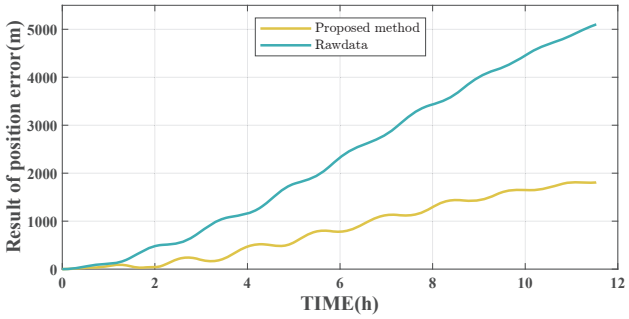

Fig. 10. Calculated position errors

Monte Carlo simulation and real experiments. The results confirm that the method proposed in this paper can efficiently estimate all error parameters and is consistent with traditional calibration results in the local-level geographical frame. Using the data before and after errors compensation, it can be found that the performance of inertial navigation after errors compensation is significantly improved. Considering the wide application of transverse frame in polar navigation, it is feasible to realize RINS polar self-calibration by using this method, which is of great significance to improve the positioning accuracy of RINS and improve the carrier navigation performance in polar region for long voyage.

REFERENCES

[1] N. El-Sheimy and A. Youssef, "Inertial sensors technologies for navigation applications: State of the art and future trends," *Satellite Navigation*, vol. 1, no. 1, p. 2, 2020.

[2] X. Mu, B. He, S. Wu, X. Zhang, Y. Song, and T. Yan, "A practical ins/gps/dvl/ps integrated navigation algorithm and its application on autonomous underwater vehicle," *Applied Ocean Research*, vol. 106, p. 102441, 2021.

[3] Y. Lin, L. Miao, Z. Zhou, and C. Xu, "A high-accuracy method for calibration of nonorthogonal angles in dual-axis rotational inertial navigation system," *IEEE Sensors Journal*, vol. 21, no. 15, pp. 16 519–16 528, 2021.

[4] C. Jekeli, *Inertial navigation systems with geodetic applications*. Walter de Gruyter GmbH & Co KG, 2023.

[5] D. Dai, Y. Ni, J. Zheng, X. Wang, and S. Qin, "Improving deflections of the vertical measurement by using rotational ins/gnss integration," in *2023 30th Saint Petersburg International Conference on Integrated Navigation Systems (ICINS)*. IEEE, 2023, pp. 1–7.

[6] L. Wang, W. Wu, J. Lian, and X. Kong, "Redundant rins information fusion with application to shipborne transfer alignment," in *2018 21st International Conference on Information Fusion (FUSION)*. IEEE, 2018, pp. 2246–2253.

[7] L. Wang, W. Wu, G. Wei, J. Li, and R. Yu, "A novel information fusion method for redundant rotational inertial navigation systems based on reduced-order kalman filter," in *MATEC Web of Conferences*, vol. 160. EDP Sciences, 2018, p. 07005.

[8] Y. Zhang, H. Luo, X. Yu, G. Wei, C. Gao, and L. Wang, "The covariance matrix transformation method in all-earth integrated navigation considering coordinate frame conversion," *Measurement Science and Technology*, vol. 33, no. 6, p. 065101, 2022.

[9] F. Qin, L. Chang, and A. Li, "Improved transversal polar navigation mechanism for strapdown ins using ellipsoidal earth model," *The Journal of Navigation*, vol. 71, no. 6, pp. 1460–1476, 2018.

[10] C. Jianhua, L. Jiaxin, and Z. Lin, "Survey on polar marine navigation and positioning system," *Chinese Journal of Ship Research*, vol. 16, no. 5, pp. 16–29, 2021.

[11] J. Cheng, J. Liu, J. Cai, and Y. Xu, "A polar integrated alignment assisted by dvl under large azimuth misalignment," *IEEE Sensors Journal*, vol. 23, no. 6, pp. 5962–5973, 2023.

[12] L.-J. Song, G.-Q. Yang, W.-L. Zhao, Y.-J. Ding, F. Wu, and X. He, "The inertial integrated navigation algorithms in the polar region," *Mathematical problems in engineering*, vol. 2020, pp. 1–9, 2020.

[13] M. Tian, Z. Liang, Z. Liao, R. Yu, H. Guo, and L. Wang, "A polar robust kalman filter algorithm for dvl-aided sins based on the ellipsoidal earth model," *Sensors*, vol. 22, no. 20, p. 7879, 2022.

[14] L. Wang, W. Wu, G. Wei, J. Lian, and R. Yu, "A polar-region-adaptable systematic bias collaborative measurement method for shipboard redundant rotational inertial navigation systems," *Measurement Science and Technology*, vol. 29, no. 5, p. 055106, 2018.

[15] Z. Wen, G. Yang, Q. Cai, and T. Chen, "An encoder-based relative attitude observation method for self-calibration in dual-axis rins," *IEEE Transactions on Industrial Electronics*, 2022.

[16] J. Li, S. Zhang, H. Yang, Z. Jiang, and X. Bai, "A fast continuous self-calibration method for fog rotational inertial navigation system based on invariant extended kalman filter," *IEEE Sensors Journal*, vol. 23, no. 3, pp. 2456–2469, 2022.

[17] J. Ban, L. Wang, Z. Liu, and L. Zhang, "Self-calibration method for temperature errors in multi-axis rotational inertial navigation system," *Optics Express*, vol. 28, no. 6, pp. 8909–8923, 2020.

[18] X. Hu, Z. Wang, H. Weng, and X. Zhao, "Self-calibration of tri-axis rotational inertial navigation system based on virtual platform," *IEEE Transactions on Instrumentation and Measurement*, vol. 70, pp. 1–10, 2021.

[19] M. Wang, L. Wang, and H. Han, "Research on innovative self-calibration strategy for error parameters of dual-axis rins," *IEEE Sensors Journal*, vol. 21, no. 24, pp. 27 918–27 927, 2021.

[20] Y. Yao, X. Xu, Y. Li, Y.-t. Liu, J. Sun, and J.-w. Tong, "Transverse navigation under the ellipsoidal earth model and its performance in both polar and non-polar areas," *The Journal of Navigation*, vol. 69, no. 2, pp. 335–352, 2016.

[21] D. Goshen-Meskin and I. Y. Bar-Itzhack, "Unified approach to inertial navigation system error modeling," *Journal of Guidance, Control, and Dynamics*, vol. 15, no. 3, pp. 648–653, 1992.

[22] L. Camberlein and F. Mazzanti, "Calibration technique for laser gyro strapdown inertial navigation systems," *Ortung Und Navigation*, pp. 1–13, 1985.